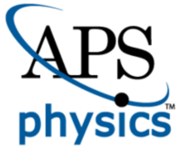

CHORUS

This is the accepted manuscript made available via CHORUS. The article has been published as:

Ultrafast carrier relaxation through Auger recombination in the topological insulator $Bi_{1.5}Sb_{0.5}Te_{1.7}Se_{1.3}$

Yoshito Onishi, Zhi Ren, Kouji Segawa, Wawrzyniec Kaszub, Maciej Lorenc, Yoichi Ando, and Koichiro Tanaka

Phys. Rev. B **91**, 085306 — Published 17 February 2015

DOI: 10.1103/PhysRevB.91.085306

Ultrafast carrier relaxation through Auger recombination in topological insulator $Bi_{1.5}Sb_{0.5}Te_{1.7}Se_{1.3}$

Yoshito Onishi[1,*], Zhi Ren[2], Kouji Segawa[2], Wawrzyniec Kaszub[3], Maciej Lorenc[3], Yoichi Ando[2,†], and Koichiro Tanaka[1,4,5,‡]

[1] *Department of Physics, Graduate School of Science, Kyoto University, Sakyo-ku, Kyoto 606-8502, Japan*

[2] *Institute of Scientific and Industrial Research, Osaka University, Ibaraki, Osaka 567-0047, Japan*

[3] *Institut de Physique de Rennes, Université de Rennes I-CNRS, UMR 6251, F-35042 Rennes, France*

[4] *Institute for Integrated Cell-Material Sciences (WPI-iCeMS), Kyoto University, Sakyo-ku, Kyoto 606-8501, Japan*

[5] *CREST, Japan Science and Technology Agency, 4-1-8, Kawaguchi, Saitama 332-0012, Japan*

Abstract

Ultrafast carrier dynamics have great significance for our understanding of the transport properties of the surface state in topological insulator (TI) materials. We report mid-infrared pump-probe measurements on the intrinsic TI material, $Bi_{1.5}Sb_{0.5}Te_{1.7}Se_{1.3}$, and show that the change in photo-induced reflectivity can be decomposed into a fast negative part and a slow positive part. Calculations of the dielectric function made at various carrier temperatures and densities reveal that the fast negative component corresponds to the disappearance of the phase-space filling effect due to hot carriers around the probe energy, and the decay component corresponds to the recombination of carriers near the band edge. The ratio of the fast negative component to the slow positive component is larger in the excitations conducted at the higher carrier densities, which suggests that the carrier temperature increases through Auger recombination. A qualitative analysis using rate equations reinforces this assumption, so we conclude that Auger recombination is the main cause of the population relaxation at carrier densities higher than 10^{18} cm^{-3}, and that we determined the Auger coefficient for $Bi_{1.5}Sb_{0.5}Te_{1.7}Se_{1.3}$ as $C = 0.4 \times 10^{-26} \mathrm{cm}^6$ /s.

PACS number: 78.47.+p, 78.20.-Ci, 71.10.-w

* Electronic address: onishi@scphys.kyoto-u.ac.jp

† Electronic address: y_ando@sanken.osaka-u.ac.jp

‡ Electronic address: kochan@scphys.kyoto-u.ac.jp

1

I. Introduction

2 The surface electronic states of three-dimensional topological insulators (TIs) follow the
3 massless Dirac equation with the spin state locked by the momentum direction as a result of the
4 nontrivial topology in the bulk insulating state [1–11]. The electronic properties of surface states have
5 been investigated with angle-resolved photoemission spectroscopy (ARPES)[7–9], tunneling
6 spectroscopy[10, 11], and conductivity measurements[12–20]. The experimental elucidation of the ultrafast
7 carrier dynamics in typical Bi_2Se_3, Bi_2Te_3, and Sb_2Te_3 TIs and their mixed crystals had a great impact
8 on our understanding of the transport properties of massless Dirac electrons and spin-polarized
9 charge current. So far, non-equilibrium carriers have been produced by near-infrared (IR) pulse
10 excitation, and their picosecond dynamics have been studied by examining the time-resolved ARPES
11 spectra[21–24] and time-resolved reflectivity [25–29]. These studies have clarified that thermalizing and
12 subsequent cooling of non-equilibrium carriers occurs after photo-excitation and quasi-steady filling
13 of the surface states arises through bulk-to-surface interband scattering[21–23,28]. These findings may
14 point the way to a novel scheme for ultrafast optical control of the surface conduction channel.
15
16 As mentioned above, time-resolved ARPES spectra measurements have revealed the
17 subsequent thermalizing and cooling processes of non-equilibrium carriers after photo-excitation. J.
18 A. Sobota et al. studied carrier thermalizing and cooling dynamics after excitation of carriers in both
19 *n*-type[21] and *p*-type[22] Bi_2Se_3 with 1.5 eV near-IR optical pulses. They found that hot carriers cool
20 down within a few picoseconds, and meta-stable bulk carriers fill the surface states through the
21 bulk-to-surface scattering. Y. Wang et al.[23] investigated the mechanism behind bulk-to-surface
22 scattering in terms of the dependence on the lattice temperature of *n*-type Bi_2Se_3 and found that the
23 bulk-to-surface scattering channel shuts off at low lattice temperature, which indicates that this
24 channel is mediated by acoustic phonon emission.
25
26 In contrast to the clear evidence for surface-state filling, the main mechanism of the carrier
27 relaxation process has yet to be determined. Under the conditions of the above experiments,
28 many-body effects such as Auger recombination originating from highly excited carriers with
29 densities of $10^{19} - 10^{20}\ \mathrm{cm}^{-3}$ should play an important role in the ultrafast relaxation process.
30 Auger recombination is the main relaxation process of the carrier population in narrow gap
31 semiconductors, wherein electrons and holes recombine non-radiatively and the recombination
32 energy is transferred to residual carriers. Since this relaxation process can compete with
33 bulk-to-surface scattering, it is important to clarify its role in the relaxation process. The time
34 constant of Auger recombination is $0.01 - 1$ ps for typical narrow-gap semiconductors InAs[30] and
35 InSb[31] at carrier densities of $10^{19} - 10^{20}\ \mathrm{cm}^{-3}$. The Bi_2Se_3 family of TIs also has a narrow bulk
36 band-gap energy (0.3 eV), so Auger recombination should be an important factor in its picosecond
37 dynamics. Auger recombination has not been discussed to much extent in the previous reports,
38 although some[24] have mentioned that this effect occurs in the initial stage of the relaxation process.

1 To understand the Auger recombination effect, the fluence dependence in the time-resolved
2 measurement should be clarified. However, in the previous time-resolved ARPES studies, carriers
3 were excited with a high fluence ($10^{19} - 10^{20}$ cm^{-3}) to obtain sufficiently strong signal to perform
4 photoemission spectroscopy, and no detailed fluence dependence of the carrier relaxation dynamics
5 has been reported. Furthermore, the excitation energy (1.5 eV) was much higher than the bulk
6 band-gap energy, and hence the dominant phenomenon contributing to hot carriers was the large
7 excess energy, not Auger recombination. Here, we studied the relaxation dynamics near the band
8 edge in order to suppress the excess energy and tried to determine whether the hot carrier distribution
9 originates from the excess energy or from Auger recombination. For this purpose, we considered that
10 TI materials with bulk-insulating properties[12–19] would be a way to distinguish the scattering
11 dynamics of the excited carriers from scattering by the originally doped carriers. Additionally, by
12 suppressing free carrier absorption, we can estimate the number of excited electron-hole pairs.
13 Bulk-insulating TI materials have recently been synthesized[12–19]. Measurements of their optical
14 properties, such as an absorption spectrum and reflection loss, are necessary for determining the
15 exact excited carrier density.
16
17 We studied the intrinsic TI material, $\mathrm{Bi}_{1.5}\mathrm{Sb}_{0.5}\mathrm{Te}_{1.7}\mathrm{Se}_{1.3}$[14,15] (carrier density of $N_{eq} =$
18 2.3×10^{16} cm^{-3} at 1.8 K). First, we measured the reflectivity spectrum from 0.15 eV to 7.0 eV and
19 obtained the broadband dielectric function and optical conductivity with Kramers-Kronig analysis.
20 Next, using these optical properties, we conducted mid-IR pump-probe reflectivity measurements.
21 We excited the carriers with mid-IR optical pulses having photon energies ranging from 0.30 eV to
22 0.66 eV, and the excited carrier density was in the range $1 \times 10^{18} - 1 \times 10^{19}$ cm^{-3}. We could
23 obtain sufficiently strong signals even from such low-density excitations owing to the high resistivity
24 of the bulk. Photo-induced reflectivity changes were measured around 0.7 eV, which is higher than
25 the excitation energy. This observation enabled us to monitor the change in the population of hot
26 carriers. From the excitation density and photon energy dependencies, we found that more hot
27 carriers were created at high excitation densities and that Auger recombination should be relevant in
28 the relaxation dynamics. Theoretical simulations with rate equations were in good accordance with
29 the experimental observations, and we concluded that in the initial stage, carriers underwent Auger
30 recombination and the remaining carriers became hot. These findings indicate that fewer bulk
31 carriers are available for surface-filling because Auger recombination affects the high-density
32 excitations and suppresses the supply of surface carriers.
33
34

35 ## II. Experiment

36 ### A. Sample Preparation

37

High-quality single crystals of $Bi_{1.5}Sb_{0.5}Te_{1.7}Se_{1.3}$ were grown by melting stoichiometric amounts of high-purity elements in sealed quartz tubes at 850 ℃ for 48 h and then cooling them slowly to 550℃, at which the boule was kept for four days to reduce crystal defects. X-ray diffraction analyses confirmed that the crystals had a chalcogen-ordered tetradymite structure. Representative crystals cut from the boules were characterized by measuring the temperature dependence of the resistivity and the low-temperature Hall coefficient; these measurements were confirmed to be similar to those reported in Refs. 9 and 12-16 for these compositions. According to the ARPES spectrum of $Bi_{1.5}Sb_{0.5}Te_{1.7}Se_{1.3}$[9], the chemical potential of electrons is above the Dirac point of the surface states between the bulk band gap at 30 K, which indicates that the surface Dirac fermions are *n*-type, and the electron density in the bulk electronic state is quite small ($N_{eq} \sim 10^{16}\ \mathrm{cm}^{-3}$).

B. Characterization of Optical Conductivity

The reflectivity measurements were performed using a Fourier-transform IR spectrometer (Bruker Optics, VERTEX 80v) with a microscope system (HYPERION) operating between 0.15 eV and 1.6 eV, a single monochromator (Princeton Instruments) with a charge-coupled device (CCD) camera (InSight100A) between 1.5 eV and 3.0 eV, and a vacuum grating monochromator of the Seya-Namioka type (Shimadzu, SGV-50) with a deuterium lamp (Hamamatsu, L1835) between 3.0 eV and 7.0 eV. Figure 1(a) shows the reflectivity spectrum $R(\omega)$ for $Bi_{1.5}Sb_{0.5}Te_{1.7}Se_{1.3}$ from 0.15 eV to 7.0 eV at room temperature (300 K). We obtained the absorption spectrum and dielectric function by applying a Kramers-Kronig transformation to the reflectivity spectrum. Before the transformation, extrapolations were made with the Drude response below 0.15 eV and with the ω^{-4}-dependence above 7.0 eV [32]. The optical conductivity for the Drude response is given by

$$\sigma_{\mathrm{D}}(\omega) = \frac{iN_{\mathrm{A}}e^2}{m^*}\frac{1}{\omega + i\gamma_D}\ , \tag{1}$$

where ε_0 is the dielectric constant of the vacuum, e is the elementary charge, N_{A} is the carrier density at the equilibrium state, m^* is the effective mass, and γ_{D} is the carrier scattering rate. The extrapolation used a free carrier density of $N_{\mathrm{A}} = 5 \times 10^{18}\ \mathrm{cm}^{-3}$ at $300\ \mathrm{K}$, the effective mass, $m^* = 0.32 m_0$[15,20](m_0 is the electron mass), for $Bi_{1.5}Sb_{0.5}Te_{1.7}Se_{1.3}$, and the carrier scattering rate for Bi_2Se_3, $\hbar\gamma_{\mathrm{D}} = 3.27\ \mathrm{meV}$[33] ($\hbar$ is the planck constant). At 300 K, the bulk electronic state of $Bi_{1.5}Sb_{0.5}Te_{1.7}Se_{1.3}$ becomes semiconducting, since holes are thermally excited from acceptor levels. These holes mainly contribute to the free carrier absorption at room temperature, and the free carrier density N_{A} at 300 K was determined using the relation $N_A = N_{\mathrm{A}}^{\mathrm{eff}} \exp(-\Delta^*/k_B T_{eq})$, where $N_{\mathrm{A}}^{\mathrm{eff}}$ is the effective acceptor density ($N_{\mathrm{A}}^{\mathrm{eff}} = 6 \times 10^{19}\ \mathrm{cm}^{-3}$)[14], Δ^* is the effective activation energy

1 $(\Delta^* = 65\ \text{meV})$[14], k_B is the Boltzmann constant, and T_{eq} is the carrier temperature at the
2 equilibrium state ($T_{eq} = 300$ K). The background dielectric constant ε_b was determined by
3 least-squares fitting and we obtained $\varepsilon_b = 19.6$. Here, the plasma frequency
4 $\hbar\omega_\text{p} = \hbar\sqrt{N_\text{A}e^2/(\varepsilon_b\varepsilon_0 m^*)}$ was estimated as $\hbar\omega_\text{p} = 32.7$ meV. The extrapolation above 7.0 eV
5 was determined by a least-squares fitting with the function, $R(\omega) = (\omega/\Omega_0)^{-4}$, and we obtained
6 $\hbar\Omega_0 = 3.8$ eV. The extrapolations are shown as the blue dashed lines in Fig. 1(a). We confirmed that
7 the extrapolations had no significant effect on the derived spectra. The real part $\varepsilon_1(\omega)$ of the
8 dielectric function $\tilde{\varepsilon}(\omega) = \varepsilon_1(\omega) + i\varepsilon_2(\omega)$ and the real part $\sigma_1(\omega)$ of the optical conductivity
9 $\sigma(\omega) = \sigma_1(\omega) + i\sigma_2(\omega)\big(= -i\varepsilon_0\omega(\tilde{\varepsilon}(\omega) - 1)\big)$, resulting from Kramers-Kronig analysis, are shown
10 in Figs. 1(c) and (d), and the penetration depth $l(\omega)$ is shown in Fig. 1(b). Note that the reflectivity
11 spectrum and the dielectric function have similar structures to those in the previous reports on the
12 Bi_2Se_3 family [34–36].
13
14
15 **C. Femtosecond Pump and Probe Experiments**
16
17 To clarify the non-equilibrium carrier dynamics, pump-probe reflectivity measurements
18 were performed with mid-IR optical pulses on single crystals of $Bi_{1.5}Sb_{0.5}Te_{1.7}Se_{1.3}$ at room
19 temperature ($T_{eq} = 300$ K). Carriers were selectively excited with mid-IR ultrafast laser pulses at
20 photon energies ranging from 0.30 eV to 0.66 eV. The mid-IR pulses were generated by the output
21 from a Ti: sapphire regenerative amplifier (Legend Elite, Coherent; central wavelength of 800 nm,
22 repetition rate of 1 kHz and pulse width of 100 fs) followed by an optical parametric amplifier
23 (TOPAS, Light Conversion) and a non-collinear difference frequency generator (NDFG, Light
24 Conversion). To monitor the population change of the hot carriers, photo-induced reflectivity
25 changes, $\Delta R(t)/R_0 = (R(t) - R_0)/R_0$, were measured around the photon energy of 0.7 eV with an
26 InGaAs photodiode, where R_0 is the reflectivity in the absence of light irradiation and $R(t)$ is that
27 after light irradiation. By selecting this probe energy, we can avoid the spatial differences in the
28 excitation density, because the penetration depth (shown in Fig. 1(b)) of the probe light is smaller
29 than that of the excitation light. Since the penetration depth at the probe energy is larger than the
30 thickness of the surface states, we will mainly discuss the dynamics of the bulk carriers. The probe
31 light was generated by the output from another Ti: sapphire regenerative amplifier (Legend USP,
32 Coherent; central wavelength of 800 nm, repetition rate of 1 kHz and pulse width of 45 fs) followed
33 by an optical parametric amplifier (TOPAS, Light Conversion). Since the seed pulses of the two
34 regenerative amplifiers were generated from one Ti: sapphire oscillator (Mira Seed, Coherent: a
35 repetition rate of 76 MHz) and synchronized with each other, there was zero temporal jitter between
36 the pump and probe pulse,[37] and the time resolution was limited by the pulse width (100 fs). All of
37 the measurements were performed at room temperature ($T_{eq} = 300$ K).

III. Time-resolved Reflectivity Measurements

A. Assignment of Optical Transitions in $Bi_{1.5}Sb_{0.5}Te_{1.7}Se_{1.3}$

In time-resolved reflectivity measurements, photo-excited carriers are thermalized on sub-picosecond order through carrier-carrier scattering[21,22]. The distribution function of the thermalized electrons (holes) is a Fermi-Dirac distribution characterized by the carrier temperature $T_{e(h)}$, which is higher than the values at thermal equilibrium just after photo-excitation in most cases, and carrier chemical potential $\mu_{e(h)}$. To calculate the change in the reflectivity spectrum in such a hot-carrier distribution, we decomposed the dielectric function at thermal equilibrium (shown in Figs. 1(c) and (d)) into several components and found the general form applicable to a hot-carrier distribution.

The optical conductivity consists of one broad structure from 0.3 to 5 eV and the extrapolated Drude response in the mid-IR region (labeled D). The structure is composed of five peaks, labeled L_0, I, L_1, L_2, and L_3 from the lower energy side (shown as Fig. 1(d)). The indirect band gap energy of $Bi_{1.5}Sb_{0.5}Te_{1.7}Se_{1.3}$[9] has been estimated from photo-emission spectra to be around $E_g^I = 0.3$ eV, which means that peak I starting from 0.3 eV should be attributed to the interband transition from the highest valence band (labeled V1) to the lowest conduction band (labeled C1). Since L_0 is on the lower energy side of I, we attributed it to the resonance of the exciton formed between V1 and C1. The remaining peaks, L_1, L_2, and L_3, should originate from the interband transitions between other electronic bands. To clarify the carrier dynamics near the band edge, we excited carriers between V1 and C1 and probed the carrier distribution in these bands with mid-IR pulses. The photon energies of the pump and probe pulses are indicated in the inset in Fig. 1(a).

For quantitative evaluations, we decomposed the structure from 0.3 to 5 eV into five absorption bands, I and L_i ($i = 0,1,2,3$). In the following, we described the optical conductivities for the five absorption bands in order to calculate the reflectivity spectra for the thermal equilibrium state and the photo-induced non-equilibrium state. Since peak I is attributed to the interband transition of our main study, we carefully determined the optical conductivity $\sigma_{\mathrm{I}}(\omega)$ including the carrier distribution. It can be written as a superposition of Lorentzian functions in k-space[38–40],

$$\sigma_{\mathrm{I}}(\omega) = -\frac{2i\omega e^2}{m_0}\int \frac{\mathrm{d}^3 k}{(2\pi)^3} \frac{f_{\mathrm{I}}\,[1 - f_{\mathrm{FD}}(E_e(\boldsymbol{k}), T_e, \mu_e) - f_{\mathrm{FD}}(E_h(\boldsymbol{k}), T_h, \mu_h)]}{\omega_{\mathrm{I}}(\boldsymbol{k})^2 - \omega^2 - i\gamma_{\mathrm{I}}\omega}, \qquad (2)$$

where f_{I} is the oscillator strength of the electric-dipole transition between C1 and V1, γ_{I} is the

1 damping constant, $\omega_{\mathrm{I}}(\boldsymbol{k})$ is the resonance frequency, and $T_{e(h)}$ and $\mu_{e(h)}$ are the temperature and
2 chemical potential for electrons (holes). The factor of 2 arises from two spin states in C1 and V1
3 bands. $f_{\mathrm{FD}}(E,T,\mu)=1/\left[\mathrm{e}^{(E-\mu)/k_BT}+1\right]$ is the Fermi-Dirac distribution at temperature T and
4 chemical potential μ. The zero point of the chemical potential μ and the energy E for electrons
5 (holes) is defined as the value at the Γ point of the C1 (V1) energy dispersion. The oscillator
6 strength f_{I} is connected with the momentum matrix element between C1 and V1, P_{CV}, through the
7 relation $f_{\mathrm{I}}=2|P_{\mathrm{CV}}|^2/(m_0\hbar\omega_I(\boldsymbol{k}))$[38]. In most cases, P_{CV} and γ_{I} do not strongly depend on $\boldsymbol{k}$ [38],
8 and therefore, we regarded them as constant parameters. $\omega_{\mathrm{I}}(\boldsymbol{k})$ was derived from the energy
9 dispersions of the electron band $E_e(\boldsymbol{k})$ and the hole band $E_h(\boldsymbol{k})$, using the relation, $\omega_{\mathrm{I}}(\boldsymbol{k})=$
10 $\left(E_e(\boldsymbol{k})+E_h(\boldsymbol{k})+E_g\right)/\hbar$, where E_g is the direct band gap energy ($E_g=0.38\ \mathrm{eV}$ [9]). An
11 appropriate model for the energy dispersions, $E_{e(h)}(\boldsymbol{k})$, was assumed to be a cosine-shape dispersion
12 in the direction of the trigonal axis (c_3 axis) and a parabolic dispersion in the direction perpendicular
13 to the trigonal axis, represented as
14

$$E_{e(h)}(\boldsymbol{k})=\frac{\hbar^2}{2m^*_{e(h),\perp}}\left(k_\perp^2-k^0_{e(h)}k_\perp\right)+\frac{1}{2}\varepsilon_{e(h)}(k_\perp,\theta)\left[1-\cos\left(\frac{c}{3}k_z\right)\right], \tag{3}$$

15
16 where c is the lattice constant ($c=2.983\ \mathrm{nm}$)[14], k_z is in the trigonal axis in k-space, $k_\perp=$
17 $\sqrt{k_x^2+k_y^2}$ is in the perpendicular direction to k_z, k_x is in the binary axis (c_1 axis), k_y is
18 perpendicular to k_z and k_x, and $\theta=\operatorname{atan}(k_x/k_y)$. Since the minima of the hole dispersion do not
19 lie at the Γ point, we added a linear term $k_h^0k_\perp$ to the first term of the right-hand side. Accounting
20 for the hexagonal warping effect[4], $\varepsilon_{e(h)}(k_\perp,\theta)$ was assumed to have the following hexagonal
21 shape: $\varepsilon_{e(h)}(k_\perp,\theta)=\varepsilon^0_{e(h)}-\beta_{e(h)}k_\perp(1-\cos 6\theta)/2$. We determined the values of these constants,
22 summarized in Table I, by referring to the band structure obtained from a first-principles
23 calculation[3,41]. A simple model for the optical conductivity $\sigma_{\mathrm{L},i}(\omega)$ for the L_i ($i=0,1,2,3$) peaks
24 is given by a Lorentzian function,
25

$$\sigma_{\mathrm{L},i}(\omega)=-\frac{i\omega\mathrm{e}^2N_{\mathrm{BZ}}}{m_0}\frac{f_i\left[1-f_{\mathrm{FD}}\left(E_{e,i},T_e,\mu_e\right)-f_{\mathrm{FD}}\left(E_{h,i},T_h,\mu_h\right)\right]}{(\omega_i)^2-\omega^2-i\gamma_i\omega}, \tag{4}$$

26
27 where N_{BZ} is the electron density over the entire Brillouin zone ($N_{\mathrm{BZ}}=1.29\times10^{22}\ \mathrm{cm}^{-3}$), derived
28 from the lattice constants ($a=0.424\ \mathrm{nm}$, and $c=2.983\ \mathrm{nm}$)[14], ω_i is the resonance frequency, f_i
29 is the oscillation strength, and γ_i is the damping constant of each Lorentzian function. $E_{e(h),i}$ is the
30 typical energy of the final (initial) state in the optical transition, assumed as $E_{e(h),i}=\left(\hbar\omega_i-E_g\right)/2$.
31
32 The dielectric function for the thermal equilibrium state or the photo-induced
33 non-equilibrium state is given by the sum of the optical conductivities as follows:
34

$$\tilde{\varepsilon}(\omega) = 1 + \frac{i}{\varepsilon_0 \omega}\left(\sigma_{\mathrm{D}}(\omega) + \sigma_{\mathrm{I}}(\omega) + \sum_{i=0}^{3} \sigma_{\mathrm{L},i}(\omega)\right). \quad (5)$$

1 In the following, we determined the parameters using a least squares analysis with Eq.(5) to the
2 dielectric function and the optical conductivity at thermal equilibrium, shown as Fig. 1(c) and (d). In
3 this fitting, we fixed the optical conductivity for the Drude response, $\sigma_{\mathrm{D}}(\omega)$, to the extrapolated
4 function. The temperatures and the carrier density were fixed to their values at room temperature
5 ($T_{e(h)} = 300$ K, $N_e^{eq} = 1 \times 10^{14}$ cm^{-3}, and $N_h^{eq} = 5 \times 10^{18}$ cm^{-3}). The values of N_e^{eq} and
6 N_h^{eq} were determined by using the relations that $N_h^{eq} - N_e^{eq} = N_A$ and $\mu_e + \mu_h + E_g = 0$ at the
7 thermal equilibrium, where the chemical potential $\mu_{e(h)}$ was derived from $N_{e(h)}^{eq}$ and $T_{e(h)} =$
8 300 K with the energy dispersion of electrons (holes). In Figs. 1(c) and (d), the best-fitting functions
9 are shown as red lines and the real parts of the optical conductivities $\sigma_{\mathrm{D}}(\omega)$, $\sigma_{\mathrm{I}}(\omega)$ and
10 $\sigma_{\mathrm{L},i}(\omega)$ $(i = 0,1,2,3)$ are shown as dotted lines. The values of the parameters are summarized in
11 Table II. The oscillator strength f_{I}, estimated from the momentum matrix element, P_{CV}, is 1.1 at
12 $\hbar\omega_I(\boldsymbol{k}) = 1$ eV. We assigned the energy structures of the peaks L_i $(i = 1,2,3)$ on the basis of the
13 previous photo-emission spectroscopy reports [21,42], as shown as Fig. 1(e). We found that the
14 calculated optical conductivity was slightly smaller than the experimental observation below the
15 band gap energy of 0.3 eV and the resonance of the exciton L_0. The slight discrepancy suggests that
16 additional optical transitions, such as interband transitions between the surface Dirac dispersions,
17 may exist below the band gap energy, and this absorption band may provide us information on the
18 optical properties in the surface states. In addition, the residual structure above 7.0 eV may originate
19 from the interband absorption between higher energy bands. The theoretical form, Eq.(5), of the
20 dielectric function and the parameters determined with the fitting were used in the analysis for the
21 photo-induced reflectivity change in the section III-D.
22
23 **B. Excitation Carrier-Density Dependence of Photo-Induced Reflectivity Change**
24
25 Figure 2(a) shows temporal profiles of the reflectivity changes $\Delta R(t)/R_0$ at excited carrier
26 densities of $\Delta N_0 = 4.2 \times 10^{18}, 8.5 \times 10^{18}, 1.3 \times 10^{19}$, and 1.7×10^{19} cm^{-3} at room
27 temperature ($T_{eq} = 300$ K). Carriers were excited at 0.61 eV, and the photo-induced reflectivity
28 change was probed at the photon energy of 0.78 eV. The excitation carrier density ΔN_0 was
29 estimated from the illuminated photon flux I, reflectivity $R(\omega)$, and penetration depth $l(\omega)$ with
30 the relation $\Delta N_0 = I\big(1 - R(\omega)\big)/l(\omega)$. In the low-density excitation, the reflectivity increased just
31 after the pulse excitation, and the reflectivity relaxed into the value at thermal equilibrium in 10 ps.
32 In contrast, in the high-density excitation, the reflectivity rapidly decreased, and the reflectivity
33 recovered with the time constant of a few picoseconds. After the reflectivity exceeded the value at
34 thermal equilibrium, it relaxed with the time constant of 10 ps. We found that the whole change
35 could be decomposed into two components: a fast-negative component and a slow-positive

component. To get a qualitative understanding of these features, we performed a least-squares fitting analysis on the reflectivity changes $\Delta R(t)/R_0$. The fitted functions were convolutions of a Gaussian function (width of 100 fs), describing the cross-correlation between the pump and probe pulses, with the double-exponential curve,

$$\frac{\Delta R(t)}{R_0} = -A_- \exp\left(-\frac{t}{\tau_-}\right) + A_+ \exp\left(-\frac{t}{\tau_+}\right), \tag{6}$$

where $A_{-(+)}$ and $\tau_{-(+)}$ are respectively the amplitude and the relaxation time of the fast negative (slow positive) component. The best-fitted functions are shown as dashed lines in Fig. 2(a). Since the relaxation time τ_+ is almost independent of the excitation photon energy, it was set to 10 ps. Figure 2(b) shows the excitation-density dependence of the ratio of the amplitudes, A_-/A_+. A_-/A_+ was smaller at lower carrier density, and it monotonously increased with carrier density. In section III-D and E, we will discuss the theoretical simulation for these results, and show the numerical results (a dotted line shown in Fig. 2(b)).

C. Excitation Photon-Energy Dependence

Figure 3(a) shows the reflectivity changes $\Delta R(t)/R_0$ probed at 0.71 eV after excitations at photon energies ranging from 0.30 eV to 0.66 eV at room temperature ($T_{eq} = 300$ K). The excited photon flux was $I = 2.8 \times 10^{14}$ cm^{-2}, which corresponds to a fluence of 30 μJ/cm^2 at 0.66 eV. After the excitation at 0.30 eV, the reflectivity rapidly increased. Then it relaxed with the lifetime of 10 ps. In contrast, at the excitation of 0.66 eV, the reflectivity rapidly decreased, then started to increase. After the reflectivity became higher than the value at thermal equilibrium, it relaxed with a time constant of 10 ps. These behaviors were quite similar to the excitation-density dependence of the photo-induced reflectivity changes. Note that the probe energy of 0.71 eV was slightly different from that of the previous measurement (0.78 eV), but we confirmed that the difference had no significant effect on the dynamics. We also applied a least-squares fitting with a double-exponential curve (6) to the photo-induced reflectivity changes. The best-fitted functions are shown as the dashed lines in Fig. 3(a). Figure 3(b) shows the excitation-energy dependence of the ratio of the amplitudes A_-/A_+ (b1), and the relaxation time τ_- (b2). We found that A_-/A_+ was almost zero at 0.30 eV, and it monotonously increased as a function of the excitation energy. The time constant of the fast-negative component, τ_-, decreased almost monotonously, although the errors of the least-squares fitting were somewhat large since the amplitude of the fast-negative component became small at the lower energy. As the excitation energy became higher, τ_- became closer to the values observed in the previous measurement at the excitation of 1.55 eV. Two possible origins for the excitation-energy dependence are conceivable. First, the dependence can be derived from the excess

1 energy transferred to carriers. Roughly, the carrier temperature T_0 just after thermalization can be
2 determined from the increase in the internal energy, obeying the relation, $\frac{3}{2}(N_A + 2\Delta N_0)k_B T_0 -$
3 $\frac{3}{2}N_A k_B T_{eq} = \Delta N_0\left(\hbar\omega - E_g^I\right)$. Here, we assume that carriers obey a Boltzmann distribution where the
4 internal energy of one free carrier $u(t)$ is given by $u(t) = 3\,k_B T(t)/2$, and that the energy
5 acquired by the photo-excitation is used for the increase in temperature of both the initial carriers
6 (density of $N_e^{eq} + N_h^{eq} \cong N_A$) and the photo-excited carriers (density of $2\Delta N_0$). The approximation,
7 $N_e^{eq} + N_h^{eq} \cong N_A$ is justified, since the electron density at the thermal equilibrium, $N_e^{eq}(= 1 \times$
8 $10^{14}\ \mathrm{cm}^{-3})$, was much smaller than the density of thermally-excited holes, N_A $(\sim 5 \times 10^{18}\ \mathrm{cm}^{-3})$.
9 The temperature of the carriers of the 0.60 eV excitation (excitation density of $\Delta N_0 = 9.1 \times$
10 $10^{18}\ \mathrm{cm}^{-3}$) was estimated to be around 1000 K, which is much higher than the lattice temperature
11 ($T_{eq} = 300$ K). Owing to the increase in carrier temperature, we observed the characteristic
12 dependence on the excitation energy. Another possibility is the increase in carrier density. Although
13 we set the excited photon flux to a constant value, the excitation carrier density depended on the
14 absorption coefficient on the photon energy, following $\Delta N_0 = I(1 - R(\omega))/l(\omega)$. The excitation
15 density was around $10^{18}\ \mathrm{cm}^{-3}$ at 0.30 eV, and around $10^{19}\ \mathrm{cm}^{-3}$ at 0.66 eV. Therefore, this
16 carrier-density dependence could induce the results shown in Fig. 3. In section III-D and E, we will
17 discuss the theoretical simulation for these results, and show the numerical results (lines shown in
18 Fig. 3(b)).
19
20 D. **Phenomenological Model for the Reflectivity Change**
21
22 Here, we will discuss the microscopic origins of the two exponential components. Figure 4
23 shows several processes in the generation and relaxation dynamics of photo-excited carriers in a
24 time-series order. The following scenario is conceivable, given the previous reports about the
25 time-resolved ARPES measurements[21–23]. After carriers are excited by optical pulses (Fig. 4(a)),
26 carriers are thermalized within a few hundred femtoseconds through electron-electron scattering[21–23]
27 (Fig. 4(b)). The thermalized carriers are characterized by a carrier distribution function, and their
28 relaxation dynamics are described by the temporal evolution of the thermodynamic parameters
29 (carrier temperature and carrier density). Now, let us consider how the thermodynamic parameters
30 evolve under the possible relaxation processes shown in Fig. 4. The carrier temperature just after the
31 photo-excitation is higher than the lattice temperature $T_{\mathrm{eq}} = 300\,K$, because carrier-phonon
32 scattering is slower than the carrier thermalization time. This hot carrier distribution cools down as a
33 result of the electron-phonon scattering within 2 ps[21,22] (Fig. 4(c)). A meta-stable population forms
34 around the band edge and the excited electrons relax to the valence band and the surface states in
35 several picoseconds[21–24,28]. The previous reports suggest that the main process of this population
36 relaxation is interband scattering into the surface states (Fig. 4(e)). However, in addition to this

interband scattering process, Auger recombination originating from highly excited carriers with a density of $10^{18} - 10^{19}\ \mathrm{cm}^{-3}$ should also play an important role in the recombination process (Fig. 4(d)). In Auger recombination, electrons and holes recombine non-radiatively, and the recombination energy is transferred to the residual carriers. Macroscopically, the carrier density decreases, and the carrier temperature increases. The typical time-scale of Auger recombination in narrow-gap semiconductors is a few picoseconds at the excitation-density of $10^{19}\ \mathrm{cm}^{-3}$[30,31]. Therefore, we supposed that Auger recombination is a possible process involved in the population relaxation. In section III-B, the ratio A_{-}/A_{+} in the reflectivity was found to show significant changes with carrier density, and this nonlinear behavior is direct evidence that many-body effects are relevant in the relaxation dynamics. The nonlinear dependence on the excited carrier density also suggests that Auger recombination may be related to the relaxation dynamics.

In the time-resolved ARPES experiments[21–23], non-equilibrium carriers were excited with densities of $10^{19} - 10^{20}\ \mathrm{cm}^{-3}$, and the fluence dependence of the carrier relaxation dynamics remains an unsolved problem. This is because photo-excitation with a high fluence ($10^{19} - 10^{20}\ \mathrm{cm}^{-3}$) is necessary for obtaining sufficient signals for photoemission spectroscopy, and time-resolved ARPES studies with low-fluence excitations still remain challenging at the moment. Therefore, the time-resolved ARPES study could not clarify the nonlinear dependence on the excited carrier density.

Note that thermal diffusion might be another population relaxation process, but its effect seems negligible in this experimental situation. The time constant of thermal diffusion, $l(\omega)^2/D$, is long, typically tens or hundreds of picoseconds at our excitation frequencies[21,22], where $l(\omega)$ is the penetration depth ($l(\omega) = 100\ \mathrm{nm} \sim 1\ \mu\mathrm{m}$; see Fig. 1 (b)), and D is the diffusion constant ($D \sim 1.2\ \mathrm{cm}^2/\mathrm{s}$ on $\mathrm{Bi_2Se_3}$ at 300 K[27]). Furthermore, although the penetration depth strongly depended on the excitation frequency, we found no significant dependence on the relaxation time of the decay component τ_{+}. Thus, we conclude that the thermal diffusion is not playing an important role. Since the time constant of radiative recombination of electron-hole pairs is typically slower than a nanosecond[21,22], this effect is also negligible on the observed time scale.

Let us discuss how this non-equilibrium carrier distribution characterized by the carrier temperature and density is related to the reflectivity. The dielectric function for a non-equilibrium carrier distribution was calculated with equations (1)-(5) by using the Fermi-Dirac distribution at a carrier temperature and density far from the values before the photo-excitation. Figure 5(a) shows the numerical simulation of the frequency dependence of the change in reflectivity from that at thermal non-equilibrium. We also show the reflectivity in Fig. 5(b), which is an enlarged view of the reflectivity spectrum in Fig. 1(a). The change in reflectivity was calculated by using the dielectric functions for non-equilibrium carrier distribution at the carrier temperature of $T_{\mathrm{e}} = T_{\mathrm{h}}$ = 800 K (red solid line) and 300 K (blue dashed line). In the calculation of both lines, the carrier density was taken to be $\Delta N_e = \Delta N_h = 1 \times 10^{19}\ \mathrm{cm}^{-3}$. The chemical potential $\mu_{e(h)}$ was derived from $N_{e(h)} =$

1 $\Delta N_e + N_{e(h)}^{eq}$ and $T_{e(h)}$ with the energy dispersion of electrons (holes). We found a significant
2 difference between 800 and 300 K in the change in reflectivity near the probe energy, as shown in
3 Fig. 5(a). This probe light concerns the optical transition from V1 to C1, according to the band
4 structure shown as Fig. 1(e). At high carrier temperature, the absorption at the probe energy of 0.71
5 eV is decreased by the phase-space filling effect[39,43], since there were hot carriers even at the probe
6 energy of 0.71 eV. Consequently, the decrease in absorption at the probe energy induces a decrease in
7 reflectivity (at the red arrow in panel (a)). In contrast, at low carrier temperature, the excited
8 electrons (holes) are only near the conduction-band bottom (valence-band top) and could not reach
9 the probe energy. Note that the optical transitions involving low-energy occupied states near the band
10 gap are forbidden according to the band structure. The phase-space filling near the conduction-band
11 bottom (valence-band top) induced the change in the dielectric function. The decrease in the
12 absorption near the band edge induced not only a decrease in reflectivity near the band edge, but also
13 an increase in reflectivity at the high energy (at the blue arrow in panel (b)). This suggests that even
14 though excited carriers decrease the absorption due to the phase-space filling, the increase or
15 decrease in reflectivity is strongly dependent on the carrier temperature. Accordingly, we assigned
16 the fast-negative component to the phase-space filling at the probe energy by hot carriers and the
17 slow-positive component to the phase-space filling near the band edge by cool carriers. Roughly
18 speaking, the time constant of the fast negative component, τ_-, can be attributed to the carrier
19 cooling time, and that of the slow positive component, τ_+, can be attributed to the carrier lifetime.
20 Note that the calculation of the dielectric function also includes a contribution from the free carrier
21 absorption in addition to the phase-space filling effect, but it was negligible at the carrier densities of
22 this study, since the plasma frequency ($\omega_\mathrm{p} = 30 - 100$ meV) of the excited free carriers was smaller
23 than the probe energy.
24
25 To make the analysis of the photo-induced reflectivity change more quantitative, we
26 evaluated the temporal profiles of the carrier temperature and density by using rate equations
27 including carrier cooling, Auger recombination, and interband scattering to the surface state. First,
28 we developed a rate equation for the carrier density. The rate equation for the excited electron (hole)
29 density $\Delta N_{e(h)}(t) = N_{e(h)}(t) - N_{e(h)}^{eq}$ can be written as follows[31,44,45]:
30

$$\frac{d}{dt}\Delta N_{e(h)}(t) = -\left(\frac{1}{\tau_N} + \frac{1}{\tau_A}\right)\Delta N_{e(h)}(t). \quad (7)$$

31
32 Here, τ_N and τ_A respectively represent time constant for interband scattering to the surface (Fig.
33 4(d)) and Auger recombination time (Fig. 4(b)). The Auger recombination rate τ_A^{-1} is dependent on
34 carrier densities and given as $\tau_A^{-1} = CN_e(t)N_h(t)$, where C is an Auger coefficient for
35 $Bi_{1.5}Sb_{0.5}Te_{1.7}Se_{1.3}$. Note that we have omitted the k-dependence of the Auger coefficient C, although
36 it is generally dependent on the energy or wavenumber of the carriers. Since the electron density at

the thermal equilibrium, $N_e^{eq}(= 1\times 10^{14}\ \mathrm{cm}^{-3})$, was much smaller than $\Delta N_{e(h)}(t)$ and N_h^{eq} ($\sim 10^{18}\ \mathrm{cm}^{-3}$), the Auger recombination rate τ_A^{-1} can be simplified as $\tau_A^{-1} = C\Delta N_e(t)(\Delta N_h(t) + N_A)$ with $N_e(t) \cong \Delta N_e(t)$, $N_h(t) \cong \Delta N_h(t) + N_\mathrm{A}$. We can obtain the relation that $\Delta N_e(t) = \Delta N_h(t)\big(= \Delta N(t)\big)$ with Eq. (7), since the density of excited electrons and holes are equal at the photo-excitation (i.e. $\Delta N_e(t = 0) = \Delta N_h(t = 0) = \Delta N_0$).

Next, we developed a rate equation for the carrier internal energy based on two assumptions: (i) the temperatures of electrons and holes are equal (i.e. $T(t) = T_e(t) = T_h(t)$), and (ii) the Auger recombination energy is equal to the sum of the band gap energy and the internal energy of one electron-hole pair. The first assumption is justified by the fact that the electron-hole scattering time should be faster than the time resolution. In this case, the rate equation for the carrier internal energy of one carrier, i.e. carrier temperature, can be written as

$$\frac{d}{dt}\left(\frac{3}{2}k_B T(t)\right) = -\frac{1}{\tau_T}\frac{3}{2}k_B\big(T(t) - T_{eq}\big) + \frac{1}{\tau_A}\left[E_g^I + 2\cdot\left(\frac{3}{2}k_B T(t)\right)\right]\frac{\Delta N(t)}{N_A + 2\Delta N(t)}, \tag{8}$$

where the first and the second terms on the right-hand side represent carrier cooling by electron-phonon scattering (τ_T: cooling time, shown as Fig. 4(c)) and energy acquisition by Auger recombination. T_{eq} is the lattice temperature, and we used $T_{eq} = 300\ \mathrm{K}$. To simplify this equation, we assumed that carriers obey a Boltzmann distribution where the internal energy of one free carrier $u(t)$ is given by $u(t) = 3\,k_B T(t)/2$. The factor of $\Delta N(t)/(N_A + 2\Delta N(t))$ in the second term is included by considering that the energy acquired through Auger recombination is distributed into whole carriers (thermally-excited holes from acceptor levels and photo-excited carriers) within the thermalization. The initial temperature T_0 was determined from the internal energy obeying the relation, $\frac{3}{2}(N_A + 2\Delta N_0)k_B T_0 - \frac{3}{2}N_A k_B T_{eq} = \Delta N_0\big(\hbar\omega - E_g^I\big)$.

E. Numerical Results

We used equations (7) and (8) to calculate the temporal profiles of the photo-induced reflectivity changes in the manner described in Fig. 5(b) of section III-D. The carrier distribution was a Fermi-Dirac distribution with density $N_e(t) = \Delta N(t)$ and $N_h(t) = \Delta N(t) + N_A$, and temperature $T(t)$ corresponding to the solutions of the rate equations. The chemical potential $\mu_{e(h)}$ was derived from $N_{e(h)}(t)$ and $T(t)$ with the energy dispersion of electrons (holes). First, to show that this model of the rate equations can reproduce the experimental results, we present numerical solutions of the photo-induced reflectivity changes at various excitation energies. Figures 6(a) and (b) show the time evolutions of the reflectivity changes at $C = 0$ and $C = 0.4\times 10^{-26}\mathrm{cm}^6\ /\mathrm{s}$ (=

C_1). C_1 is of the same order as the Auger coefficients of narrow gap semiconductors, such as InSb ($C = 1.2 - 1.7 \times 10^{-26}\mathrm{cm}^6\ /\mathrm{s}$[31], gap energy of 0.17 eV) and InAs ($C = 1.0 - 1.2 \times 10^{-26}\mathrm{cm}^6\ /\mathrm{s}$[30], gap energy of 0.35 eV). Here, τ_N and τ_T are 15 and 0.4 ps, respectively. At $C = 0$ shown in Fig. 6(a), under the high-energy photo-excitation (a1), there was a small positive peak at $t = 0$ in the reflectivity change, and then $\Delta R(t)/R_0$ rapidly decreased just after the photo-excitation. After this rapid decrease, $\Delta R(t)/R_0$ recovered with the time constant of a few picoseconds, and then relaxed with the time constant of 10 ps. In the low-energy excitation (a7), $\Delta R(t)/R_0$ increased just after the photo-excitation, and then relaxed. With the same decomposition-analysis in the section III-B and C, the fast components shown in Fig. 6(a) were much smaller than those obtained in the experiment. In contrast, at $C = C_1$ shown in Fig. 6(b), the fast negative components became more prominent as the excitation energy increased, which indicates that Auger recombination enhanced the carrier temperatures at the higher energy excitation. These calculated reflectivity changes were in good qualitative accord with the measured reflectivity changes shown in Fig. 3(a). Note that small positive peaks are seen at $t = 0$ in panels a1-a4 and b1-b4 of Fig. 6, but they are not observed in the experiment. This is probably due to the breaking of the assumption that the carriers are immediately thermalized in each time steps. Actually, the carriers are thermalized with a finite time constant, which might smooth these sharp peaks. Since this breaking of the assumption is relevant only at the initial stage of the carrier relaxation dynamics, it does not have any essential effect on the following discussion about the carrier dynamics after the thermalization.

The temporal profiles of $\Delta N(t)$ and $\Delta T(t) = T(t) - T_{eq}$ (Figs. 6(c) and (d)) clearly indicate the carrier dynamics. Without Auger recombination, both density and temperature decreased exponentially (panel (c)). Note that the difference in carrier density at $t = 0$ was caused by the dependence of the absorption coefficient on the excitation energy. In contrast, when the effect of Auger recombination was included, the carrier density after the high energy excitation decreased more rapidly before it asymptotically approached an exponential decay (panel (d)). In the previous ARPES observations of Bi_2Se_3 at room temperature[21,23], the population relaxation time was slower than $1/\Gamma_{\mathrm{esc}} < 2$ ps. In our calculation, the rapid population relaxation was due to Auger recombination in the initial stage, which is consistent with the previous observations. The Auger recombination increased the carrier temperature. At the high carrier temperatures resulting from Auger recombination, the photo-induced reflectivity change became negative; then, the reflectivity change increased as the carriers relaxed into thermal equilibrium. Furthermore, we found that the relaxation dynamics could not be simply described as a single exponential decay. The analytical solution in the long-time limit ($\mathrm{t} \gg \tau_{\mathrm{N}}, \tau_{\mathrm{T}}$, $E_g^{\mathrm{I}} \gg k_B \Delta T(t)$, and $N_A \gg \Delta N(t)$) enables us to understand this nontrivial behavior. In this limit, the solution for the carrier density is given as $\Delta N(t) \cong \Delta N_1 e^{-t/\tau_N}$, where $\Delta N_1 = \Delta N_0/[1 - C\tau_N N_A \Delta N_0]$. The rate equation for the carrier temperature follows a double-exponential decay, $T(t) \cong T_{eq} + \Delta T_1 \exp(-2t/\tau_N) + \Delta T_2 \exp(-t/$

1 $\tau_T)$, where $\Delta T_1 = C(\Delta N_1)^2 T_3(1/\tau_T - 2/\tau_N)^{-1}$, $T_3 = 2E_g/3k_B + 2T_{\rm eq}$ and $\Delta T_2 = T_0 - T_{eq} -$
2 ΔT_1. The decay time of the slow component is determined by the carrier density relaxation time and
3 the amplitude is proportional to the Auger coefficient, which suggests that the carriers acquire the
4 excess energy due to Auger recombination of residual carriers. The cooling became slower as a result
5 of the Auger recombination, and it is consistent with the temporal profile observed in the ARPES
6 measurements[21–24]. This slow-positive component was also observed in the previous ARPES
7 measurement[21,22]. According to the solution for the carrier density in the long-time limit, Auger
8 recombination becomes dominant at carrier densities larger than $\Delta N_0 = 1/(C_1 \tau_N N_A)$, which, given
9 the parameters of the simulation, is 3×10^{18} cm^{-3}. Therefore, we observed a prominent change in
10 the photon energy dependence because the excited carrier density in our study was comparable with
11 this threshold value.
12
13 As a more quantitative investigation, a least-squares fitting with a double-exponential curve
14 (6) was applied to the calculated reflectivity changes as well as the experimental reflectivity changes.
15 The best-fitting curves are shown as the dashed lines in Fig. 6(b), and the fitting parameters, A_-/A_+
16 (b1) and τ_- (b2), are plotted in Fig. 3 (b). To determine the value of the Auger coefficient for
17 $Bi_{1.5}Sb_{0.5}Te_{1.7}Se_{1.3}$, we examined A_-/A_+ and τ_- for three cases: $C = 0.5C_1$ (dashed lines), C_1
18 (solid lines), and $2C_1$ (dotted lines). At the higher excitation energy, A_-/A_+ became larger and the
19 time-constant τ_- became faster as in the experimental results. Note that as the Auger coefficient
20 became larger, the fast-negative component became more prominent. We found that the deviation at
21 the excitation of 0.48 eV was larger than that at other photon energy, which can probably be due to
22 the measurement error, such as a wrong measurement of photon energy. Furthermore, we compare
23 the experimental excitation-density dependences with the initial carrier dependence of A_-/A_+
24 calculated with this model (the dotted line) in Fig. 2(b). This result reproduced the experimental
25 behavior very well. Given these trends, we choosed $C = C_1$ as the value of the Auger coefficient.
26 Note that the value of the Auger coefficient for $Bi_{1.5}Sb_{0.5}Te_{1.7}Se_{1.3}$, $C = 0.4 \times 10^{-26}$cm^{-3}, is
27 smaller than the values for other narrow-gap semiconductors, InSb ($C = 1.2 - 1.7 \times 10^{-26}$cm^6 /s[31])
28 and InAs ($C = 1.0 - 1.2 \times 10^{-26}$cm^6 /s[30]). This should be due to the difference in effective mass.
29 Since the effective mass for $Bi_{1.5}Sb_{0.5}Te_{1.7}Se_{1.3}$ (electron mass: $0.32m_0$[15,20]) is larger than those of
30 InSb (electron mass: $0.015m_0$[46]) and InAs (electron mass: $0.026m_0$[46]), the energy conservation law
31 is more difficult to be satisfied.
32
33 In our study, the initial carrier density depended on the penetration depth, following
34 $\Delta N_0 = I(1 - R(\omega))/l(\omega)$, as well as on the excitation photon energy. Therefore, we should clarify
35 whether Auger recombination at high carrier densities or excess photon energy is responsible for the
36 remarkable decrease in reflectivity. Here, we simulated the dependence of $\Delta R(t)/R_0$ on the
37 excitation energy for various initial carrier densities. Figure 7(a) shows the results for initial carrier
38 densities of $\Delta N_0 = 1 \times 10^{18}$ (a1), 2×10^{18} (a2), 4×10^{18}(a3), and 8×10^{18}cm^{-3}(a4). As the

photon energy increased, the fast-negative component became more pronounced than the slow-positive components, but the size of this change decreased as the carrier density increased. Thus, we consider that the increase in carrier density mainly contributed to the increase in the carrier temperature. We calculated the temporal profiles in the situation where we selectively changed the excitation energy at carrier densities ranging from 10^{18} to $10^{19}\,\mathrm{cm}^{-3}$. We also applied a least-squares fitting with a double-exponential curve to the temporal profiles. The photon energy dependencies of A_{-}/A_{+} as a result of the fitting analysis are shown in Fig. 7(b). Here, we show again both experimental and numerical results of the excitation-energy dependence of A_{-}/A_{+} which have been already shown in panel b1 of Fig. 3. This figure also indicates that the size of the increase in relation to the carrier density was larger than that in relation to the photon energy.

IV. Conclusion

In summary, we studied the relaxation dynamics near the band edge in an intrinsic TI material, $Bi_{1.5}Sb_{0.5}Te_{1.7}Se_{1.3}$, by conducting mid-IR pump-probe reflectivity measurements. We demonstrated that the temporal profile of the photo-induced reflectivity change has a nonlinear dependence on the excited carrier density, which suggests that many-body effects play an important role in the relaxation dynamics. On the basis of the excitation photon-energy dependence, we decomposed the temporal profiles into fast negative and slow positive components and concluded that these components correspond to the relaxations of carrier temperature and density by referring to the previous time-resolved measurements. Numerical solutions of the rate equations for the carrier temperature and density revealed that the Auger recombination process could be an essential relaxation process after the photo-excitation, in addition to thermalization, cooling, and population relaxation. By comparing the numerical solutions with the experimental results, we decided the Auger coefficient as $C = 0.4 \times 10^{-26}\mathrm{cm}^6\,/s$. These new findings on Auger recombination point to interesting many-body physics in TI materials.

Acknowledgements

Y.O. thanks I. Akimoto of Wakayama University and M. Shirai of Kyoto University for their help in measuring the ultraviolet spectrum of $Bi_{1.5}Sb_{0.5}Te_{1.7}Se_{1.3}$. Y.O. acknowledges support by the Japan–Europe–US International Training Program for Young Generation in Molecular Materials Science for Development of Molecular Devices. K.T. acknowledges support by a Grant-in-Aid for Scientific Research on Innovative Areas, titled ‘Optical science of dynamically correlated electrons (DYCE)’ (Grant No. 20104007), and a Grant-in-Aid for Scientific Research (A) (Grant No. 26247052). Y.A. acknowledges support by a Grant-in-Aid for Scientific Research on Innovative

1 Areas, titled ‘Topological Quantum Phenomena’ (Grant No. 22103004), a Grant-in-Aid for Scientific
2 Research (S) (Grant No. 25220708), and the Air Force Office of Scientific Research of the USA
3 (Grant No. AOARD 124038). W. K. and M. L. acknowledge support by Rennes Métropole, ANR
4 (ANR-13-BS04-0002), and Fonds Européen de Développement Régional (FEDER).
5
6
7
8

1 **References**

2 [1] M.Z. Hasan and C.L. Kane, Rev. Mod. Phys. **82**, 3045 (2010).
3 [2] Y. Ando, J. Phys. Soc. Jpn. **82**, 102001 (2013).
4 [3] H. Zhang, C.-X. Liu, X.-L. Qi, X. Dai, Z. Fang, and S.-C. Zhang, Nat. Phys. **5**, 438 (2009).
5 [4] L. Fu, Phys. Rev. Lett. **103**, 266801 (2009).
6 [5] H.-Z. Lu, W.-Y. Shan, W. Yao, Q. Niu, and S.-Q. Shen, Phys. Rev. B **81**, 115407 (2010).
7 [6] X.-L. Qi and S.-C. Zhang, Rev. Mod. Phys. **83**, 1057 (2011).
8 [7] Y.L. Chen, J.G. Analytis, J.-H. Chu, Z.K. Liu, S.-K. Mo, X.L. Qi, H.J. Zhang, D.H. Lu, X. Dai, Z.
9 Fang, S.C. Zhang, I.R. Fisher, Z. Hussain, and Z.-X. Shen, Science **325**, 178 (2009).
10 [8] D. Hsieh, Y. Xia, D. Qian, L. Wray, J.H. Dil, F. Meier, J. Osterwalder, L. Patthey, J.G. Checkelsky,
11 N.P. Ong, A.V. Fedorov, H. Lin, A. Bansil, D. Grauer, Y.S. Hor, R.J. Cava, and M.Z. Hasan, Nature
12 **460**, 1101 (2009).
13 [9] T. Arakane, T. Sato, S. Souma, K. Kosaka, K. Nakayama, M. Komatsu, T. Takahashi, Z. Ren, K.
14 Segawa, and Y. Ando, Nat. Commun. **3**, 636 (2012).
15 [10] Z. Alpichshev, J.G. Analytis, J.-H. Chu, I.R. Fisher, Y.L. Chen, Z.X. Shen, A. Fang, and A.
16 Kapitulnik, Phys. Rev. Lett. **104**, 016401 (2010).
17 [11] P. Cheng, C. Song, T. Zhang, Y. Zhang, Y. Wang, J.-F. Jia, J. Wang, Y. Wang, B.-F. Zhu, X. Chen,
18 X. Ma, K. He, L. Wang, X. Dai, Z. Fang, X. Xie, X.-L. Qi, C.-X. Liu, S.-C. Zhang, and Q.-K. Xue,
19 Phys. Rev. Lett. **105**, 076801 (2010).
20 [12] Z. Ren, A.A. Taskin, S. Sasaki, K. Segawa, and Y. Ando, Phys. Rev. B **82**, 241306(R) (2010).
21 [13] K. Segawa, Z. Ren, S. Sasaki, T. Tsuda, S. Kuwabata, and Y. Ando, Phys. Rev. B **86**, 075306
22 (2012).
23 [14] Z. Ren, A.A. Taskin, S. Sasaki, K. Segawa, and Y. Ando, Phys. Rev. B **84**, 165311 (2011).
24 [15] A.A. Taskin, Z. Ren, S. Sasaki, K. Segawa, and Y. Ando, Phys. Rev. Lett. **107**, 016801 (2011).
25 [16] A.A. Taskin, S. Sasaki, K. Segawa, and Y. Ando, Phys. Rev. Lett. **109**, 066803 (2012).
26 [17] C. Brüne, C.X. Liu, E.G. Novik, E.M. Hankiewicz, H. Buhmann, Y.L. Chen, X.L. Qi, Z.X. Shen,
27 S.C. Zhang, and L.W. Molenkamp, Phys. Rev. Lett. **106**, 126803 (2011).
28 [18] J. Zhang, C.-Z. Chang, Z. Zhang, J. Wen, X. Feng, K. Li, M. Liu, K. He, L. Wang, X. Chen, Q.-K.
29 Xue, X. Ma, and Y. Wang, Nat. Commun. **2**, 574 (2011).
30 [19] Z. Ren, A.A. Taskin, S. Sasaki, K. Segawa, and Y. Ando, Phys. Rev. B **85**, 155301 (2012).
31 [20] C.S. Tang, B. Xia, X. Zou, S. Chen, H.-W. Ou, L. Wang, A. Rusydi, J.-X. Zhu, and E.E.M. Chia,
32 Sci. Rep. **3**, 3513 (2013).
33 [21] J.A. Sobota, S.-L. Yang, D. Leuenberger, A.F. Kemper, J.G. Analytis, I.R. Fisher, P.S. Kirchmann,
34 T.P. Devereaux, and Z.-X. Shen, J. Electron Spectrosc. Relat. Phenom. **195**, 249 (2014).
35 [22] J.A. Sobota, S. Yang, J.G. Analytis, Y.L. Chen, I.R. Fisher, P.S. Kirchmann, and Z.-X. Shen, Phys.
36 Rev. Lett. **108**, 117403 (2012).
37 [23] Y.H. Wang, D. Hsieh, E.J. Sie, H. Steinberg, D.R. Gardner, Y.S. Lee, P. Jarillo-Herrero, and N.
38 Gedik, Phys. Rev. Lett. **109**, 127401 (2012).

1 [24] A. Crepaldi, B. Ressel, F. Cilento, M. Zacchigna, C. Grazioli, H. Berger, P. Bugnon, K. Kern, M.
2 Grioni, and F. Parmigiani, Phys. Rev. B **86**, 205133 (2012).
3 [25] J. Qi, X. Chen, W. Yu, P. Cadden-Zimansky, D. Smirnov, N.H. Tolk, I. Miotkowski, H. Cao, Y.P.
4 Chen, Y. Wu, S. Qiao, and Z. Jiang, Appl. Phys. Lett. **97**, 182102 (2010).
5 [26] C.W. Luo, H.J. Wang, S.A. Ku, H.-J. Chen, T.T. Yeh, J.-Y. Lin, K.H. Wu, J.Y. Juang, B.L. Young, T.
6 Kobayashi, C.-M. Cheng, C.-H. Chen, K.-D. Tsuei, R. Sankar, F.C. Chou, K.A. Kokh, O.E.
7 Tereshchenko, E.V. Chulkov, Y.M. Andreev, and G.D. Gu, Nano Lett. **13**, 5797 (2013).
8 [27] N. Kumar, B.A. Ruzicka, N.P. Butch, P. Syers, K. Kirshenbaum, J. Paglione, and H. Zhao, Phys.
9 Rev. B **83**, 235306 (2011).
10 [28] S. Sim, M. Brahlek, N. Koirala, S. Cha, S. Oh, and H. Choi, Phys. Rev. B **89**, 165137 (2014).
11 [29] L. Cheng, C. La-o -vorakiat, C.S. Tang, S.K. Nair, B. Xia, L. Wang, J.-X. Zhu, and E.E.M. Chia,
12 Appl. Phys. Lett. **104**, 211906 (2014).
13 [30] K.L. Vodopyanov, H. Graener, C.C. Phillips, and T.J. Tate, Phys. Rev. B **46**, 13194 (1992).
14 [31] V. Chazapis, H.A. Blom, K.L. Vodopyanov, A.G. Norman, and C.C. Phillips, Phys. Rev. B **52**,
15 2516 (1995).
16 [32] T. Katsufuji, Y. Okimoto, T. Arima, Y. Tokura, and J.B. Torrance, Phys. Rev. B **51**, 4830 (1995).
17 [33] S.V. Dordevic, M.S. Wolf, N. Stojilovic, H. Lei, and C. Petrovic, J. Phys. Condens. Matter **25**,
18 075501 (2013).
19 [34] D.L. Greenaway and G. Harbeke, J. Phys. Chem. Solids **26**, 1585 (1965).
20 [35] V.V. Sobolev, S.D. Shutov, Y.V. Popov, and S.N. Shestatskii, Phys. Status Solidi B **30**, 349 (1968).
21 [36] A. Akrap, M. Tran, A. Ubaldini, J. Teyssier, E. Giannini, D. van der Marel, P. Lerch, and C.C.
22 Homes, Phys. Rev. B **86**, 235207 (2012).
23 [37] M. Lorenc, C. Balde, W. Kaszub, A. Tissot, N. Moisan, M. Servol, M. Buron-Le Cointe, H.
24 Cailleau, P. Chasle, P. Czarnecki, M.L. Boillot, and E. Collet, Phys. Rev. B **85**, 054302 (2012).
25 [38] P. Yu and M. Cardona, *Fundamentals of Semiconductors: Physics and Materials Properties*, 4th ed.
26 2010 edition (Springer, Berlin ; New York, 2010).
27 [39] J.-Y. Bigot, V. Halté, J.-C. Merle, and A. Daunois, Chem. Phys. **251**, 181 (2000).
28 [40] H. Ehrenreich and M.H. Cohen, Phys. Rev. **115**, 786 (1959).
29 [41] X. Luo, M.B. Sullivan, and S.Y. Quek, Phys. Rev. B **86**, 184111 (2012).
30 [42] V.A. Greanya, W.C. Tonjes, R. Liu, C.G. Olson, D.-Y. Chung, and M.G. Kanatzidis, J. Appl. Phys.
31 **92**, 6658 (2002).
32 [43] A.J. Sabbah and D.M. Riffe, Phys. Rev. B **66**, 165217 (2002).
33 [44] S. Hausser, G. Fuchs, A. Hangleiter, K. Streubel, and W.T. Tsang, Appl. Phys. Lett. **56**, 913 (1990).
34 [45] S. Ghosh, P. Bhattacharya, E. Stoner, J. Singh, H. Jiang, S. Nuttinck, and J. Laskar, Appl. Phys.
35 Lett. **79**, 722 (2001).
36 [46] C. Kittel, *Introduction to Solid State Physics*, 8 edition (Wiley, Hoboken, NJ, 2004).
37
38

1 **Figure Captions**

2 **Fig. 1 (Color online).** (a) Reflectivity spectrum $R(\omega)$ of $Bi_{1.5}Sb_{0.5}Te_{1.7}Se_{1.3}$ from 0.15 eV to 7.0 eV
3 at room temperature (black solid line). The blue dashed lines show extrapolation functions. The
4 extrapolation below 0.15 eV was made with the Drude response for a carrier density of $5 \times$
5 10^{18} cm^{-3}, damping constant of 3.27 meV, and high-energy dielectric constant of $\varepsilon_b = 19.6$. The
6 extrapolation above 7.0 eV was made with the function, $R(\omega) = (\omega/\Omega_0)^{-4}$ where $\Omega_0 = 3.8$ eV.
7 The inset is an enlarged view of the reflectivity spectrum between 0.15 eV and 1.2 eV. (b)
8 Penetration depth $l(\omega)$, (c) real part $\varepsilon_1(\omega)$ of dielectric function $\tilde{\varepsilon}(\omega)$, and (d) real part $\sigma_1(\omega)$ of
9 optical conductivity $\sigma(\omega)$, estimated with Kramers-Kronig analysis for $R(\omega)$ (black solid lines).
10 The red solid lines indicate the best-fitted function to $\tilde{\varepsilon}(\omega)$ with the dielectric function of Eq. (5).
11 The dotted lines indicate the components of the real parts of the optical conductivities decomposed
12 into the Drude response D, the Lorentzian functions L_i $(i = 0,1,2,3)$, and the interband transition I
13 of Eq. (2). (e) Schematic diagrams of electronic dispersions of $Bi_{1.5}Sb_{0.5}Te_{1.7}Se_{1.3}$. As the value of the
14 Fermi energy (E_F), we used that at 300 K.
15
16 **Fig. 2 (Color online).** (a) Temporal profiles of the reflectivity changes at excited carrier densities of
17 $4.2 \times 10^{18}, 8.5 \times 10^{18}, 1.3 \times 10^{19}$, and 1.7×10^{19} cm^{-3} at room temperature. The dashed lines
18 are the best-fitting functions that are convolutions of a Gaussian function with
19 double-exponential-decay curves. The vertical solid line is the zero line of the delay time. The
20 horizontal solid lines indicate the zero lines of the photo-induced reflectivity changes. (b) The filled
21 squares indicate the excitation-carrier-density dependencies of A_-/A_+ at the excitation energy of
22 0.61 eV. The photo-induced reflectivity was theoretically calculated as Fig. 7(a) (see the section
23 III-E), and we obtained the numerically calculated excitation-carrier-density dependence of A_-/A_+
24 (dotted line) at the excitation energy of 0.61 eV by applying the least-squares fitting to the
25 photo-induced reflectivity.
26
27 **Fig. 3 (Color online).** (a) Time characteristics of photo-induced reflectivity changes, $\Delta R(t)/R_0$, at
28 0.71 eV for excitations with various photon energies ((a1) 0.66, (a2) 0.60, (a3) 0.54, (a4) 0.48, (a5)
29 0.42, (a6) 0.36 and (a7) 0.30 eV) at room temperature (open circles). The dashed lines are the
30 best-fitting functions. The fitting function is a convolution of the intensity temporal profile of the
31 excitation light pulse with a double-exponential-decay curve. The scales of the vertical axes were
32 modified to make the time characteristics of$\Delta R(t)/R_0$ clear. The vertical solid lines are the zero
33 lines of the delay times. The horizontal solid lines are the zero lines of the photo-induced reflectivity
34 changes. (b) Photon-energy dependence of the ratio of the amplitude of the fast negative component
35 and the slow positive component, A_-/A_+ (panel b1) and that of the time constant of the fast
36 negative component, τ_- (panel b2). A_-/A_+ and τ_- were determined by a least-squares fitting to
37 the temporal profiles of $\Delta R(t)/R_0$ measured in the experiment (filled circles) and theoretically
38 calculated with the rate equations for Auger coefficients $C = 0.5C_1$ (green dashed lines), C_1 (black

1 solid lines), and $2C_1$ (orange dotted lines), where $C_1 = 0.4 \times 10^{-26} \mathrm{cm}^6$ /s. The photo-induced
2 reflectivity was theoretically calculated as Fig. 6(b) (see the section III-E), and we obtained the
3 numerically calculated the excitation-energy dependence of A_-/A_+ (black solid lines) by applying
4 the least-squares fitting to the photo-induced reflectivity.
5
6 **Fig. 4 (Color online).** Schematic diagrams of subsequent relaxation processes of photo-excited
7 carriers in the lowest conduction band (C1), the highest valence band (V1), and the surface states
8 (SS). The possible processes are (a) photo-excitation of electron-hole pairs, (b) carrier thermalization,
9 (c) carrier cooling due to phonon emission, (d) Auger recombination, and (e) interband scattering
10 from C1 and V1 to SS.
11
12 **Fig. 5 (Color online).** (a) Frequency dependence on the photo-induced reflectivity change, $\Delta R/R_0$,
13 calculated at the carrier density of $\Delta N_0 = 1 \times 10^{19}$ cm^{-3} and carrier temperatures of $T_0 = 800$ K
14 (red solid line) and 300 K (blue dashed line). The vertical dashed line indicates the probe energy. The
15 horizontal solid line is the zero lines of the photo-induced reflectivity change. (b) Reflectivity
16 spectrum $R(\omega)$ of $Bi_{1.5}Sb_{0.5}Te_{1.7}Se_{1.3}$ from 0.3 eV to 1.0 eV at room temperature (black solid line).
17
18 **Fig. 6 (Color online).** Temporal profiles of photo-induced reflectivity changes, $\Delta R(t)/R_0$,
19 calculated with rate equations for the carrier density, Eq. (7) and for the carrier temperature, Eq. (8)
20 at $C = 0$ (a) and $C = C_1$ ($C_1 = 0.4 \times 10^{-26} \mathrm{cm}^6$ /s) (b) after photo-excitations of various
21 frequencies ((a1, b1) 0.66, (a2, b2) 0.60, (a3, b3) 0.54, (a4, b4) 0.48, (a5, b5) 0.42, (a6, b6) 0.36 and
22 (a7, b7) 0.30 eV). The dashed lines are their best-fitting functions using a convolution of a Gaussian
23 function with a double-exponential-decay curve. The scales of the vertical axes were modified to
24 make the time characteristics of $\Delta R(t)/R_0$ clear. Temporal profiles of density (c1, d1) and
25 temperature (c2, d2) calculated with the rate equations at $C = 0$ (c) and $C = C_1$ (d). The vertical
26 solid lines are the zero lines of the delay times. The horizontal solid lines in Fig. 6 (a) and (b) are the
27 zero lines of the photo-induced reflectivity changes. The dotted horizontal lines in Fig. 6 (c) and (d)
28 indicate the noise levels estimated from the signal-to-noise ratio of the reflectivity changes.
29
30 **Fig. 7 (Color online).** (a) Temporal profiles of photo-induced reflectivity changes, $\Delta R(t)/R_0$,
31 calculated in the situation where the excitation energy was selectively changed at the excitation
32 energies of 0.36 eV (blue lines), 0.48 eV (green lines), and 0.66 eV (red lines) and the excited carrier
33 density was fixed to $\Delta N_0 = 1 \times 10^{18}$ (a1), 2×10^{18} (a2), 4×10^{18} (a3), or $8 \times 10^{18} \mathrm{cm}^{-3}$ (a4).
34 The vertical solid lines are the zero lines of the delay times. (b) Excitation-energy dependencies of
35 A_-/A_+ calculated at fixed excited carrier densities in the range $\Delta N_0 = 1 \times 10^{18} - 10 \times 10^{18}$ cm^{-3}
36 (solid lines). The filled circles and dashed line respectively indicate the excitation-energy
37 dependencies of A_-/A_+ estimated from the experimental observations and calculated under the
38 same conditions as in the experiment. The filled circles and dashed line are the same as those shown

in panel (b1) of Fig.3.

Table Captions

Table I. Corrections to the values of parameters for the electronic dispersions C1 and V1 of $Bi_{1.5}Sb_{0.5}Te_{1.7}Se_{1.3}$.

Table II. Corrections to the values of parameters for the electronic transitions concerning peaks I, D, L_0, L_1, L_2, and L_3.

1 **Fig. 1**

2

3

4

5

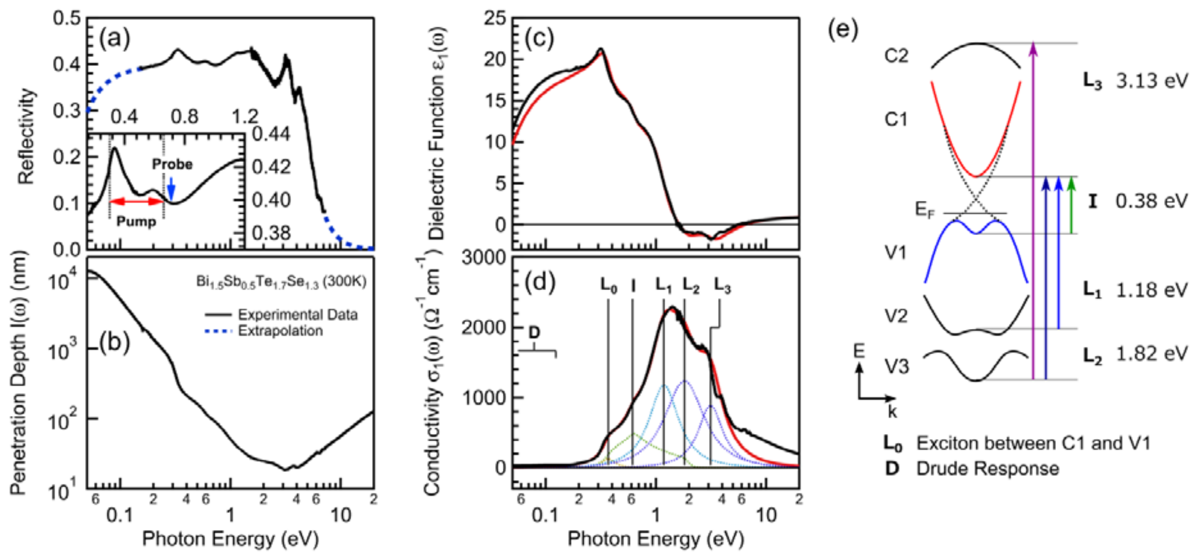

6

7

8

9

10

11

12 **Y. Onishi et al.**

13

1 **Fig. 2**

2

3

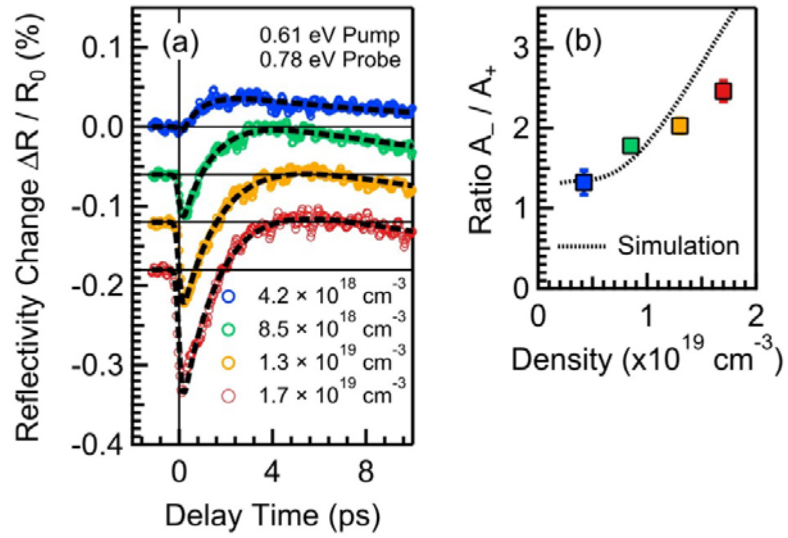

4

5

6

7

8 **Y. Onishi et al.**

9

1 **Fig. 3**

2

3

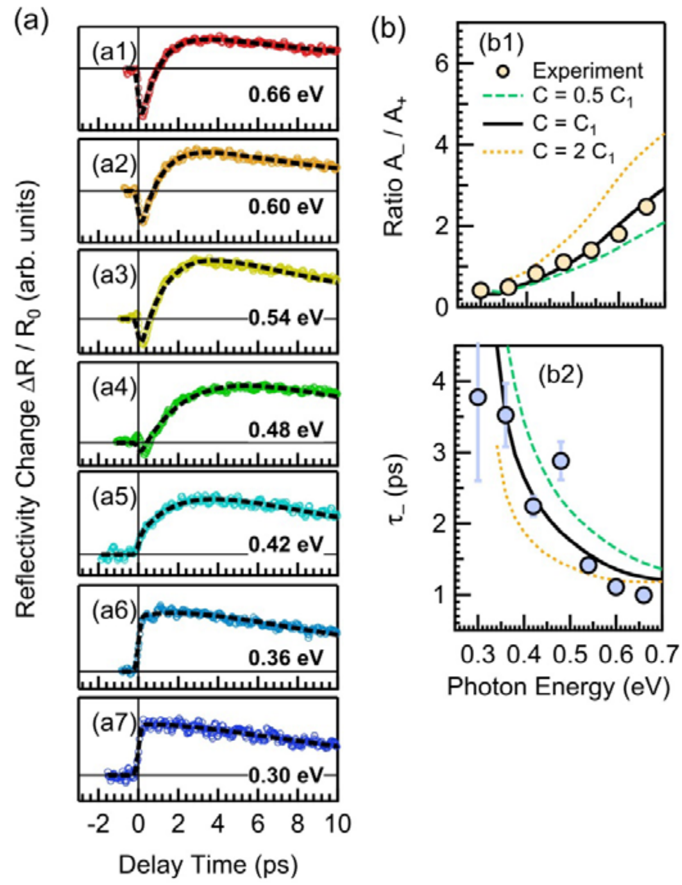

4

5

6

7

8 **Y. Onishi et al.**

9

1 **Fig. 4**

2

3

4

5

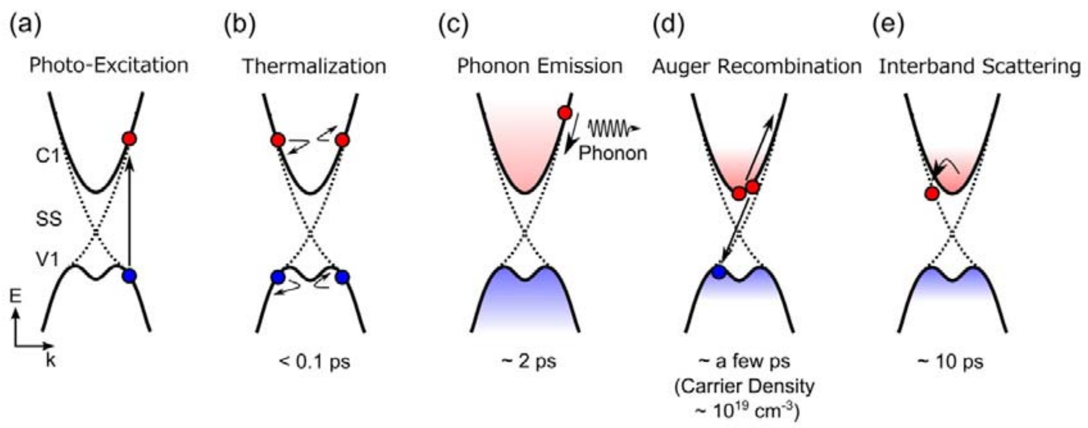

6

7

8

9

10

11

12 **Y. Onishi et al.**

13

1 **Fig. 5**

2

3

4

5

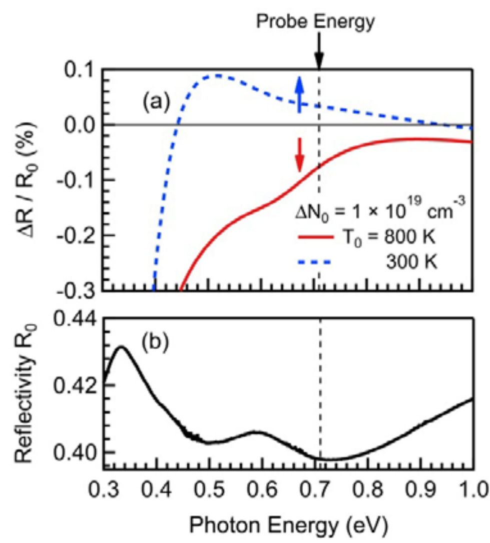

6

7

8

9

10

11

12 **Y. Onishi et al.**

13

1 **Fig. 6**

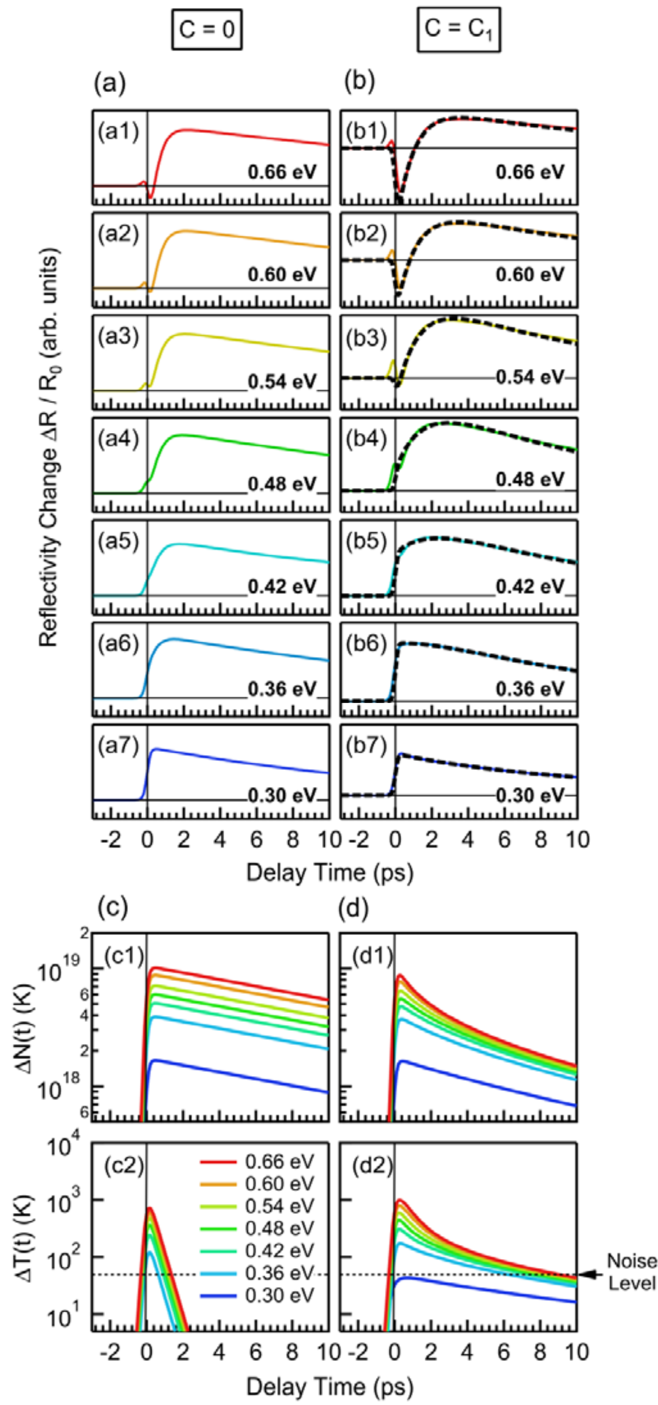

2

3 **Y. Onishi et al.**

4

1 **Fig. 7**

2

3

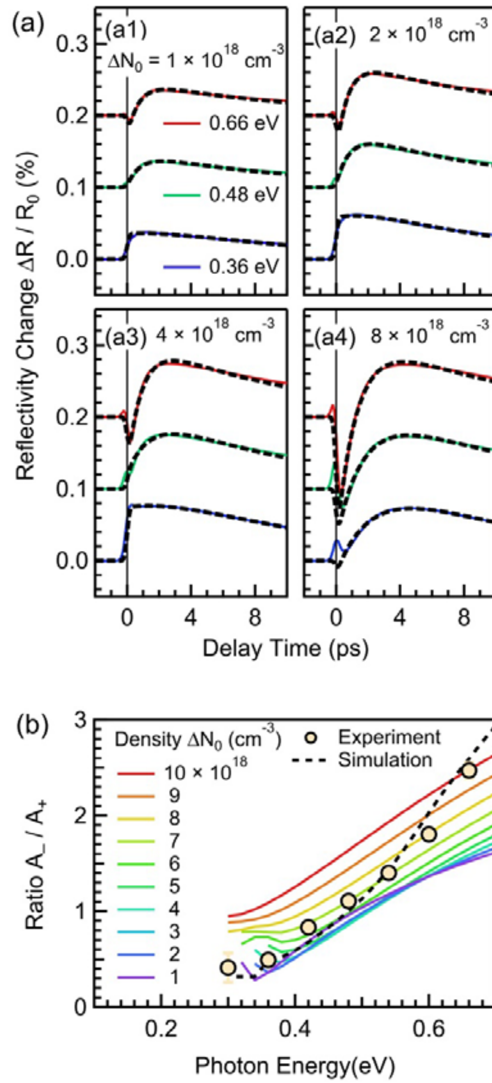

4

5

6 **Y. Onishi et al.**

7

1 **Table I.**

2

3

4

5

6

Parameters	Electron (e)	Hole (h)
$m^*_{e(h),\perp}/m_0$	0.32	0.30
$k^0_{e(h)}$ (nm^{-1})	0	1.10
$\varepsilon^0_{e(h)}$ (eV)	0.05	0.03
$\beta_{e(h)}$ (eV · nm)	0.04	0.03

7

8

9

10

11

12

13

14

15 **Y. Onishi et al.**

16

Table II.

Band	Parameters	Values
I	$\hbar\gamma_I$ (eV)	0.10
	P_{CV} (keV/c)	0.53
D	$\hbar\omega_P$ (meV)	32.7
	$\hbar\gamma_D$ (meV)	3.27
L_0	$\hbar\omega_0$ (eV)	0.37
	$\hbar\gamma_0$ (eV)	0.12
	f_0	7.5×10^{-3}
L_1	$\hbar\omega_1$ (eV)	1.18
	$\hbar\gamma_1$ (eV)	0.89
	f_1	0.44
L_2	$\hbar\omega_2$ (eV)	1.82
	$\hbar\gamma_2$ (eV)	1.84
	f_2	0.95
L_3	$\hbar\omega_3$ (eV)	3.13
	$\hbar\gamma_3$ (eV)	1.97
	f_3	0.73

Y. Onishi et al.